Zeolite Synthesized from Solid Waste for Eco-System Remediation: Selective Adsorption in Wastewater

Mariana S. Araujo [1],*, Danilo Costa-Silva [1], Juliana C. Izidoro [2], Denise A. Fungaro [2] and Sonia Mello Castanho [1]

[1] Centro de Ciência e Tecnologia dos Materiais, Instituto de Pesquisas Energéticas e Nucleares, São Paulo 05508-000, SP, Brazil; danilo.silva@ipen.br (D.C.-S.); srmello@ipen.br (S.M.C.)

[2] Centro de Química e Meio Ambiente, Instituto de Pesquisas Energéticas e Nucleares, São Paulo 05508-000, SP, Brazil; dfungaro@ipen.br (D.A.F.)

* Correspondence: mariana.araujo@ipen.br; Tel.: +55-(11)-2810-1691

Abstract: The present investigation explores the potential of two synthesized zeolites, derived from coal fly ash (CFA; thermoelectric waste) and sugarcane bagasse ash (SCBA; agro-industrial waste), for the selective adsorption of cesium in wastewater. The synthesized zeolites (ZCFA and ZSCBA) were characterized and compared with a commercial zeolite to evaluate their physicochemical properties and effectiveness in removing cesium ions (Cs^+) from simulated radioactive wastewater. The results obtained from X-ray diffraction, scanning electron microscopy, and elemental analysis confirmed the successful synthesis of high-purity zeolite from both solid wastes. The impurities present in the ashes impacted the Si/Al ratio and consequently influenced the exchange capacity. After adsorption experiments, neutron activation analysis (NAA) revealed that ZSCBA adsorbed 33.4% of Cs_2O by weight, outperforming both ZCFA (26.0%) and commercial zeolite (27.9%). The superior performance of ZSCBA is attributed to its distinct Si/Al ratio and lower levels of impurities, highlighting the impact of these factors on adsorption selectivity. The findings in this study demonstrate the feasibility of valorizing agro-industrial waste for synthesizing zeolites, offering a sustainable approach for managing these residues while producing valuable materials for environmental remediation.

Keywords: zeolite; coal fly ash; sugarcane bagasse ash; cesium adsorption; radioactive wastewater treatment

1. Introduction

The global drive towards sustainable development and ecosystem remediation necessitates innovative solutions for managing complex environmental challenges, particularly in nuclear energy and radioactive waste management. With the International Atomic Energy Agency projecting a 120% increase in nuclear electricity production capacity by 2050, addressing the safe management of radioactive effluents containing radionuclides like cesium-137 (137Cs) has become essential for protecting and rehabilitating affected ecosystems [1,2].

Synthetic zeolites represent a promising technological intervention for environmental remediation, particularly for the removal of radioactive cesium from wastewater. Zeolites, crystalline aluminosilicates with a microporous structure, large surface area, and uniform pore size, represent a promising solution for environmental remediation. The material's general formula $Me_{2/n}O \cdot Al_2O_3 \cdot xSiO_2 \cdot yH_2O$ enables versatile applications in water purification through adsorption processes [3].

Among them, Zeolite A (also known as Linde Type A, LTA) has gained particular attention due to its unique structural features and excellent ion-exchange properties. This zeolite possesses a characteristic structure composed of sodalite cages (β-cages) connected by double four-member rings (D4R), leading to the formation of large cavities separated by eight-member rings (8R) called windows. The Si/Al ratio close to 1 and the high aluminum content in its framework create more negative charges that need to be balanced by exchangeable cations, making it particularly effective for removing radioactive cations from wastewater [4].

There are three main synthesis routes to obtain zeolites: conventional hydrothermal treatment in a single step, alkali fusion followed by hydrothermal treatment, and a two-step process involving silicon extraction followed by a reaction with external aluminum sources [5]. Among these, conventional hydrothermal synthesis involves adding alkali to aluminum and silicon sources in appropriate proportions in an aqueous medium under controlled temperature, achieving around 50% conversion of raw materials into zeolites. While the alkali fusion method can produce higher-purity products, the silicon extraction route can yield specific zeolite phases, and the hydrothermal route offers advantages in terms of the process's simplicity and scalability [6].

The hydrothermal synthesis route, while widely recognized, involves critical parameters that significantly influence material properties like temperature, reaction time, and Si/Al ratio, which directly impact the textural characteristics of zeolites and their adsorption capabilities [7].

Recent studies by Nasser et al. [8] demonstrated significant advancements in zeolite synthesis through microwave-assisted hydrothermal methods, achieving enhanced crystallinity and controlled morphology. Park et al. [9] further optimized crystallization parameters using fusion/hydrothermal methods, establishing crucial relationships between synthesis conditions and zeolite performance.

Furthermore, the development of cost-effective synthesis methods using industrial wastes has gained significant attention, particularly using coal fly ash (CFA) and other waste materials [6,10,11]. Fan et al. [12] showed that zeolites synthesized from CFA can serve dual purposes—waste utilization and environmental remediation.

Experimental studies have confirmed that zeolite-based materials, such as zeolite X/activated carbon composite, can achieve substantial adsorption rates of around 40.7 mg/g [13]. Additionally, Ybañez et al. [14] successfully prepared clinoptilolite nanozeolite using silica derived from sugarcane bagasse ash, achieving higher nutrient loading (9.62% N and 17.01% K_2O content) compared to commercial natural zeolite.

Building upon previous research, Belviso [15] comprehensively reviewed zeolite synthesis processes from coal and biomass fly ash, highlighting the importance of controlled synthesis conditions for optimal performance. Zou et al. [16] investigated the fundamental factors influencing adsorption mechanisms, particularly focusing on the role of surface chemistry and pore size. The methodology developed by Izidoro et al. demonstrated remarkable reproducibility and potential for expansion across various ash types [17–21].

The present study presents novel contributions to the field of environmental remediation and radioactive waste treatment. While previous studies have focused on single waste sources or different applications, this research is the first to systematically compare zeolite A synthesis from two abundant industrial waste streams: coal fly ash (CFA) and sugarcane bagasse ash (SCBA) specifically for Cs+ removal from radioactive wastewater. The availability of these materials in Brazil—approximately 2 million tons of coal fly ash and 10 million tons of sugarcane bagasse ash annually [22–24]—provides an ideal opportunity to develop a cost-effective and sustainable solution that addresses both waste management and nuclear safety challenges. This research bridges critical knowledge gaps

by investigating the comparative cesium absorption capacity of zeolites derived from these two waste sources, offering insights into how different precursor materials affect the final product's performance.

The primary research objectives are: (1) to synthesize Zeolite A through a standardized hydrothermal method [18] using coal fly ash and sugarcane bagasse ash as precursors; (2) to comprehensively characterize the physicochemical properties of the resulting zeolites, with particular focus on properties that influence cesium adsorption; (3) to evaluate their effectiveness in removing cesium ions from simulated radioactive wastewater, benchmarking their performance against commercial Zeolite A. The novelty of this work lies in its comprehensive three-way comparison between zeolites derived from two distinct industrial waste streams and commercial Zeolite A. This systematic comparison not only advances our understanding of waste-derived zeolite synthesis but also provides practical insights into how these sustainable alternatives perform relative to established commercial standards, offering valuable data for potential industrial applications in nuclear waste management.

## 2. Materials and Methods

2.1. Raw Materials

Two industrial solid wastes from different types of Brazilian plants served as sources of silica: coal fly ash (CFA) from a plant in Santa Catarina, Brazil, and sugarcane bagasse ash (SCBA) from a plant in Franca, São Paulo, Brazil. Both residues were characterized for their chemical composition, crystalline phases, functional groups, and morphology using various techniques, as detailed in Section 2.4 Sodium hydroxide (97%), sodium aluminate (99.99%), and cesium chloride ($\geq$99.999%), all from Sigma-Aldrich Pty. Ltd. (São Paulo, Brazil), were used in zeolite synthesis and the preparation of the simulated effluent. A commercial zeolite (4A) from Diatom Mineração Ltd.(São Paulo, Brazil) was also characterized for comparative purposes.

2.2. Synthesis of Na-A Zeolites from Industrial Solid Wastes

The synthesis was performed via a conventional hydrothermal method, following procedures described in previous studies [17,18]. Twelve grams (12 g) of NaOH were ground and mixed with 10 g of the selected industrial solid waste. The mixture was heated to 550 °C for 1 h in a porcelain crucible. The resulting material was ground and rapidly transferred to a Teflon vessel with 150 mL of distilled water and sodium aluminate in quantity sufficient to adjust the molar ratio of SiO_2/Al_2O_3 to 2.4. The suspension was aged for 2 h under stirring and then sealed and stored at 100 °C for 3 h. Afterward, the product was filtered, washed with 1 L of deionized water, and dried overnight at 105 °C. The obtained samples were labeled as ZCFA and ZSCBA for the zeolites synthesized from coal fly ash (CFA) and sugarcane bagasse ash (SCBA), respectively. This process is schematically represented in Figure 1.

2.3. Adsorption Experiments

A simulated nuclear effluent containing Cs^+ ions was prepared by dissolving 5 g of CsCl (Sigma-Aldrich Pty. Ltd.) in 500 mL of deionized water, adapting a procedure from Tian and Sasaki [25]. To prepare contaminated zeolites, 5 g of each zeolite sample was mixed with the simulated nuclear effluent and stirred for 24 h. The suspension was then filtered, and the collected solids were dried overnight at 105 °C. The contaminated samples were labeled Cs-CFA and Cs-SCBA.
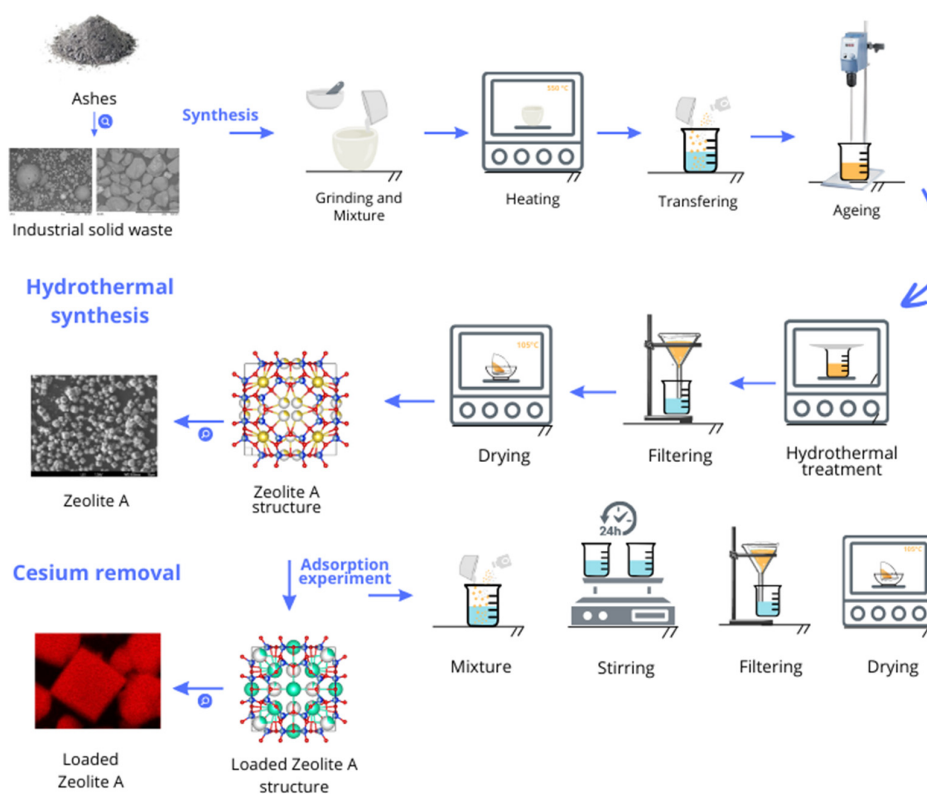
Figure 1. Schematic representation of the process employed in this study.

2.4. Characterizations

For a semi-quantitative determination of the chemical compounds present in the residue and zeolites, chemical analyses were carried out on an energy-dispersive X-ray fluorescence spectrometer (ED-XRF) SHIMADZU EDX 720, Shimadzu Corporation, Kyoto, Japan. The fundamental parameters (FPs) method was employed for analyzing the powder samples. Neutron activation analysis (NAA) was utilized to quantify the amount of Cs adsorbed by the zeolites. The samples were irradiated at IEA-R1 the nuclear research reactor located in IPEN (Instituto de Pesquisas Energéticas e Nucleares) for 8 h with a thermal neutron flux of $1012 \text{ cm}^{-2} \cdot \text{s}^{-1}$ and, then, the radionuclide 134Cs was counted using gamma spectrometry after 15 days. The accuracy of the NAA method was validated by analyzing a certified reference material (USGS STM-2) [21]. X-ray diffraction (XRD) analyses were conducted to identify the crystalline phases present in the materials. These analyses were performed using a Rigaku SmartLab, Bruker, Camarillo, CA, USA, diffractometer operating in the theta-2theta configuration, employing CuKα radiation (λ = 1.5406 Å). The X-ray diffraction data were recorded with a step size of 0.05° per second. Fourier transform infrared (FT-IR) spectroscopy was employed to evaluate the functional groups present in the materials. The spectra were recorded using a Thermo Nicolet Nexus 670 spectrometer, Thermo Electron Scientific Instruments Corporation, Livermore, CA, USA, with a spectral resolution of 0.125 cm^{-1}. Samples were prepared by dispersing pulverized glass in a KBr matrix and pressing the mixture into pellets under a vacuum. Scanning electron microscopy (SEM) was conducted to examine the morphology of the zeolite samples. A Quanta FEG 650 FEI microscope, Thermo Fisher Scientific, U.S., operating at 15 kV was used for imaging the fly ashes samples, while a Jeol JSM-6701F microscope, Japan Electron Optics Laboratory Co., Tokyo, Japan, operating at 6 kV was employed for analyzing the zeolite samples.

The zero point charge (pH_{PCZ}) of the zeolites was determined using the immersion method. A 1 L stock solution of 0.1 M NaCl was prepared and adjusted to pH values ranging from 1 to 13. Next, 20 mL aliquots of each solution were then mixed with 0.020 g

of zeolite and equilibrated for 1 h with constant homogenization. The pH of each solution was measured again (final pH) and the difference between the final and initial pH values (ΔpH) was calculated. The pHPCZ was determined as the point where the plot of ΔpH versus initial pH crossed the *x*-axis (ΔpH = 0). The specific surface area (S_{BET}) of the zeolites was determined using nitrogen adsorption at 77 K and the Brunauer–Emmett–Teller (BET) method. Adsorption-desorption isotherms were obtained using Micromeritics ASAP 2020, Micromeritics Instrument Corporation, U.S., volumetric adsorption analyzer over a relative pressure range (P/P_0) from 0.01 to 0.99. Cation exchange capacity (CEC) was measured by sequentially saturating 1.0 g samples with 100 mL of 1 mol$\cdot$L^{-1} sodium acetate, then 100 mL of 1 mol$\cdot$L^{-1} ammonium acetate. The solutions were agitated at room temperature for 24 h at 120 rpm for both solutions. After filtering and washing, the released sodium was measured using Flame Modular ICP-OES, SPECTRO, AMETEK Inc., Meerbusch, Germany. The sodium concentration was converted from mg/L to meq/g to determine the CEC value.

3. Results and Discussion

3.1. Characterization of the Fly Ashes

The chemical properties of solid industrial waste are known to be influenced by various factors, including geographical location, burning conditions (in the case of ash), and handling and storage procedures. Nevertheless, a generally consistent compositional range can be expected for both byproducts used in this study. Table 1 presents the chemical compositions of coal fly ash (CFA) and sugarcane bagasse ash (SCBA) as determined by X-ray fluorescence spectroscopy.

Table 1. Chemical composition (weight%) obtained using X-ray fluorescence spectroscopy of all materials studied.

| Sample	SiO_2	Al_2O_3	Fe_2O_3	CaO	Na_2O	K_2O	Other	L.O.I. *	Si/Al
CFA	47.8	24.5	6.0	11.7	-	2.8	5.5	2.0	1.95
SCBA	83.7	4.8	5.8	-	-	-	3.5	2.0	17.43
STD-4A	34.4	30.7	0.0	0.0	13.6	-	0.0	21.3	1.12
ZCFA	35.4	29.8	3.7	4.8	10.2	-	1.8	14.2	1.19
ZSCBA	33.2	31.3	1.6	0.1	17.4	-	0.6	15.8	1.06

* Loss on ignition.

As expected, in both, fly ashes silica (SiO_2) and alumina (Al_2O_3) are the main components [19,22]. However, the proportions of each compound differ significantly between the two materials. CFA comprises 47.8 wt% silica and 24.5 wt% alumina, while SCBA consists of 83.7 wt% and 4.8 wt% of these oxides, respectively.

Besides silica and alumina, iron oxide, along with trace amounts of other metal oxides, was detected. Both materials exhibited a loss on ignition (LOI) of 2 wt%. Furthermore, consistent with its classification as Class F fly ash, the CFA contained 11.7 wt% calcium oxide (CaO).

Changes in the crystalline structures of the materials were observed using X-ray diffraction, and the patterns are presented in Figure 2.

The diffraction patterns reveal differences in the degree of crystallinity between the ashes. CFA displays a partially amorphous structure characterized by a broad diffraction hump between 18° and 30° 2θ. Intense peaks corresponding to quartz and other sharp peaks associated with mullite, hematite, and magnetite are also observed. In contrast, SCBA exhibits a more crystalline structure, with prominent peaks attributed to quartz and mullite.
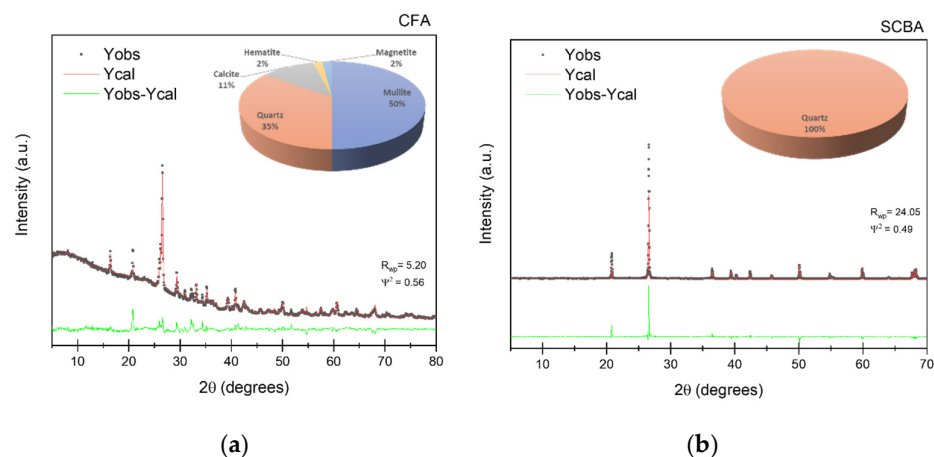
Figure 2. Rietveld refinement of X-ray diffraction patterns of (**a**) coal fly ash (CFA) and (**b**) sugarcane bagasse ash (SCBA).

The difference in the degree of crystallinity is also demonstrated using Fourier transform infrared (FT-IR) spectroscopy. Figure 3 shows the FT-IR spectra of CFA and SCBA; bands associated with quartz predominate, where, although the functional groups are in a similar region, the peaks are sharper for the SCBA sample.
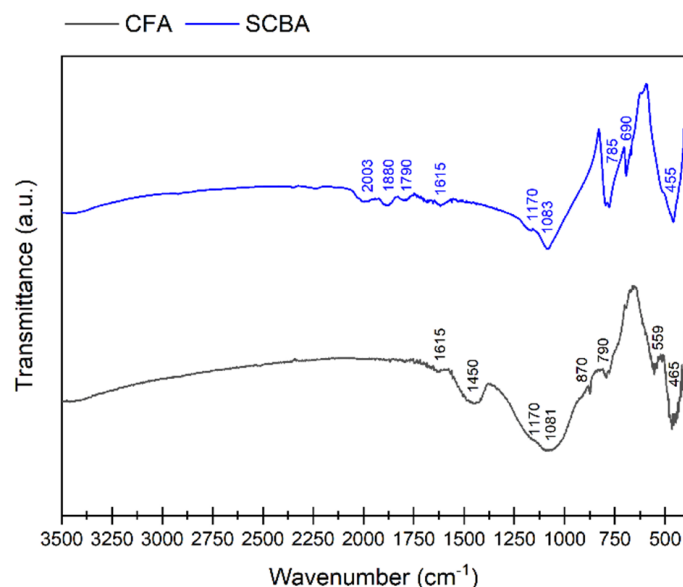

Figure 3. FT-IR spectra of coal fly ash (CFA) and sugarcane bagasse ash (SCBA).

Three regions of interest are observed in both spectra: (1) around $1615\ cm^{-1}$, attributed to H–O–H bending vibrations; (2) from 1000 to $1600\ cm^{-1}$, associated with Si–O–Si bonds; and (3) around $600\ cm^{-1}$, assigned to Si–O–Al vibrations [26]. Peaks at 870 and $1450\ cm^{-1}$, can also be observed for CFA spectra, which are associated with Ca vibrations. The sulfur content present in CFA, normally associated with calcium as calcium sulfate, can be observed at $555\ cm^{-1}$.

Scanning electron microscopy analysis was performed on both as-received samples, and the micrographs, along with the granulometric analysis, are presented in Figure 4.

As shown in Figure 4, the CFA particles exhibited predominantly spherical shapes with varying sizes, consistent with previous reports [19]. The granulometric analysis revealed a variation in particle diameter, ranging from 2 to 16 μm, with an average diameter of 5 μm. In contrast to the spherical morphology of CFA, the SCBA particles exhibited an irregular morphology, with angular and pointed ends characteristic of quartz. The granulometric

analysis of SCBA showed a broader particle size distribution, ranging from 97 to 302 µm, with an average diameter of 187 µm.
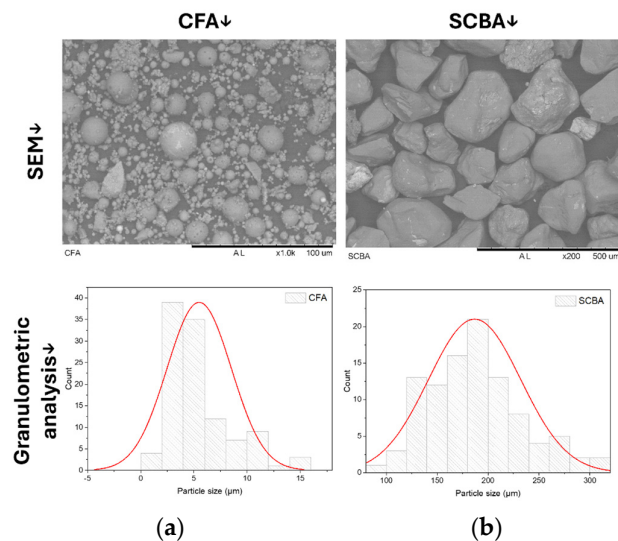
Figure 4. Scanning electron micrographs (SEM) and granulometric analysis of (**a**) coal fly ash (CFA) and (**b**) sugarcane bagasse ash (SCBA).

3.2. Characterization of the Zeolites

Hydrothermal synthesis, the method used in this study, is a multiphasic crystallization process strongly influenced by factors such as temperature, crystallization time, and the quantity of aluminum. Variations in these factors can easily induce the formation of undesired phases. Figure 5 presents the X-ray diffraction patterns of the zeolite samples before the adsorption experiments.
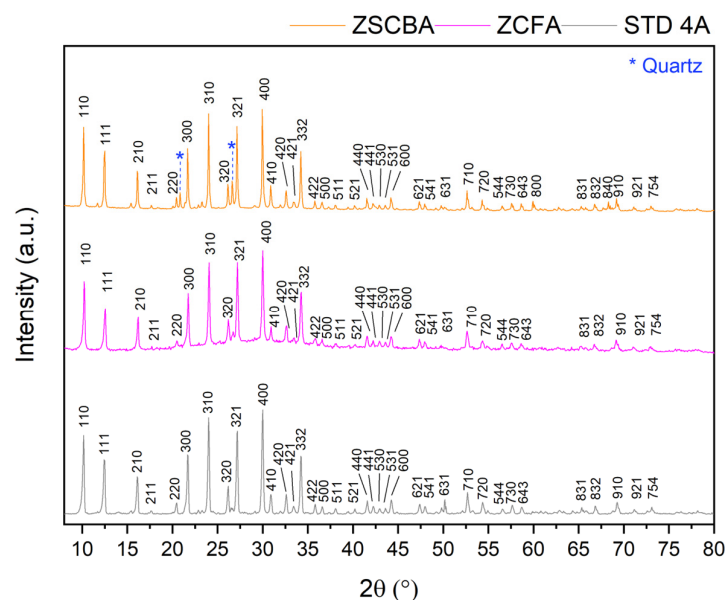
**Figure 5.** X-ray diffraction patterns of the zeolites STD-4A, ZCFA, and ZSCBA.

The XRD patterns of the zeolites confirm the successful synthesis of zeolite 4A, as evidenced by the presence of characteristic peaks corresponding to this phase (00-810-3633) [27]. This zeolite, also known as Linde Type A (LTA), possesses a unique structure composed of sodalite cages interconnected by double 4-rings in a cuboidal arrangement. In its dehydrated sodium form (4A), the chemical formula is $[Na_{12}Al_{12}Si_{12}O_{48}]_8$.

The presence of aluminum atoms introduces negative charges that are balanced by exchangeable sodium cations, which partially obstruct the micropores and give the zeolite its characteristic pore size of approximately 4.1 Å. The presence of quartz identified in the ZSCBA is due to the high degree of crystallinity of this compound in the SCBA fly ash, which probably did not react completely during the synthesis.

Figure 6 displays the scanning electron microscopy (SEM) micrographs and Gaussian particle size distributions of the synthesized and commercial zeolites.

The observation of crystals with cubic morphology and slightly varied sizes is indicative of the presence of type A zeolite characteristics. Remarkably, despite the significant disparity in the average particle size of the initial fly ashes and without undergoing any beneficiation processes, the synthesized zeolites display a narrow particle size distribution similar to that of STD-4A. Specifically, the average particle sizes of ZCFA, ZSCBA, and STA-4A are measured at 0.20 μm, 0.46 μm, and 0.16 μm, respectively. This uniformity in particle size distribution across different zeolite samples underscores the robustness of the synthesis process and highlights the potential for consistent product quality, irrespective of variations in raw material properties.

Analyzing the elemental compositions obtained using X-ray fluorescence (Table 1) for zeolites STD-4A, ZCFA, and ZSCBA reveals distinct characteristics for each sample, reflecting the variations in their precursor materials. As expected for type A zeolites, where the ideal Si/Al ratio is 1 [28], the measured Si/Al ratios ranged from 1.06 to 1.19.
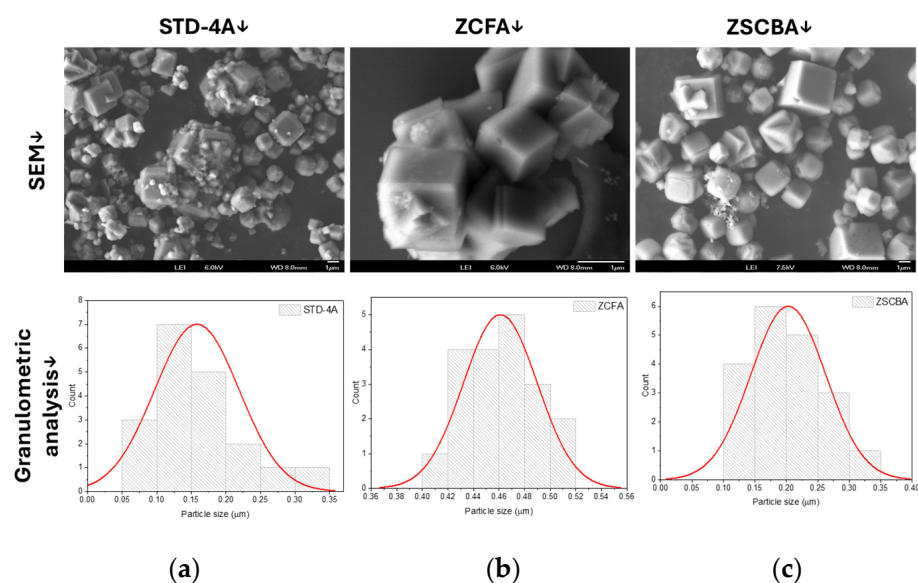
Figure 6. Scanning electron micrographs (SEM) and granulometric analysis of the zeolites STD-4A (**a**), ZCFA (**b**), and ZSCBA (**c**).

The sodium content is related to its incorporation into the zeolite structure during hydrothermal synthesis, where NaOH acts as an activating agent. ZSCBA exhibited the highest sodium content, while ZCFA had the lowest. The presence of iron oxide (Fe_2O_3) in both synthesized zeolites (ZCFA and ZSCBA) stems from their respective fly ash compositions, with ZCFA showing a higher Fe_2O_3 concentration compared to ZSCBA. Notably, calcium oxide (CaO) was found exclusively in the ZCFA sample. The presence of these oxides (Fe_2O_3 and CaO) confirms the incorporation of elements from the starting materials.

The loss on ignition (LOI) values varied among the samples, with STD-4A exhibiting the highest percentage (21.3 wt%) and ZCFA the lowest (14.2 wt%). These variations suggest differences in the amounts of volatile components or residual organic matter present in the zeolite structures.

Figure 7a,b presents the pH$_{PCZ}$ determination and pH equilibrium curves, respectively, for the STD-4A, ZCFA, and ZSCBA zeolites. The pH$_{PCZ}$ values, determined from the intersection of the ΔpH versus initial pH curves with the *x*-axis (ΔpH = 0) in Figure 7a, were found to be approximately 10 for all three zeolites. This is consistent with the pH equilibrium curves shown in Figure 7b, where the final pH values converge around pH 10, regardless of the initial pH. While the pH$_{PCZ}$ values are similar, the distinct trends in both the ΔpH curves (Figure 7a) and the pH equilibrium curves (Figure 7b) suggest variations in the nature and abundance of surface functional groups. For instance, the steeper slope of the ZCFA curve in Figure 7b at lower pH values may indicate a higher concentration of acidic surface sites compared to STD-4A and ZSCBA.

Table 2 presents the specific surface area (S$_{BET}$), the cation exchange capacities (CEC), and the amount of Cs adsorbed by the zeolites obtained using neutron activation analysis (NAA).

Table 2. Physicochemical properties of the zeolites.

Sample	S$_{BET}$ (m^2/g)	CEC (meq·g^{-1})	Cs$_2$O (wt%) *
STD-4A	255 [29]	3.14	27.9
ZCFA	193	3.15	26.0
ZSCBA	212	2.31	33.4

* Adsorption content of cesium obtained using neutron activation analysis (NAA).
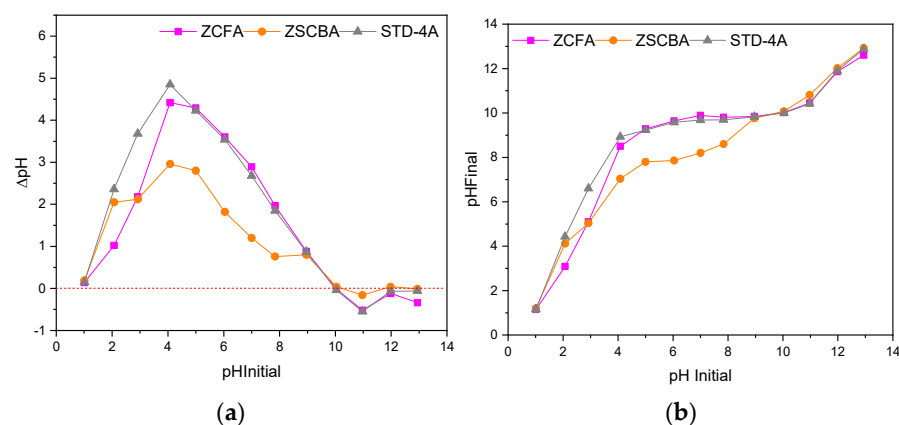
Figure 7. Immersion pH$_{PZC}$ plots: (**a**) ΔpH vs. initial pH for pH$_{PCZ}$ determination of STD-4A, ZCFA, and ZSCBA zeolites; (**b**) pH equilibrium curves (final pH vs. initial pH) for the zeolites.

The observed differences in CEC among the synthesized zeolites and commercial STD-4A reflect variations in their respective chemical compositions. Ion exchange capacity is a critical parameter for evaluating zeolite effectiveness in various applications, particularly in water treatment. Even slight variations in CEC values can significantly impact their performance.

The relatively higher CEC of STD-4A and ZCFA compared to ZSCBA suggests that STD-4A and ZCFA may possess more accessible exchange sites or larger pore sizes, facilitating the uptake of ions from the solution. This could be attributed to the differences in the composition of the precursor materials and/or the presence of specific impurities, such as iron oxide in ZCFA, which may influence the ion exchange behavior and contribute to the observed variations in CEC values.

Neutron activation analysis (NAA) revealed significant variations in cesium content among the contaminated zeolite samples. Cs-ZSCBA demonstrated the highest cesium concentration (33.4 wt%), indicating greater adsorption efficiency compared to Cs-STD-4A (27.9 wt%) and Cs-ZCFA (26.0 wt%). These differences likely arise from variations in zeolite

structure, chemical composition, surface area, and porosity, all of which influence the materials' adsorption capacity and selectivity towards cesium ions.

Furthermore, the specific surface area (SBET) of the synthesized zeolites ZCFA and ZSCBA, determined by nitrogen adsorption (BET method), was found to be 193 m^2/g and 212 m^2/g, respectively. These values are more consistent with the SBET for a commercial zeolite 4A (STD-4A), which is 255 m^2/g [29], than with the SBET reported for a zeolite synthesized using coal fly ash from a thermal power plant in China (121 m^2/g) [25]. It is important to note that the zeolite synthesized in the Chinese study was produced under similar conditions to those used in the present work, suggesting that other parameters may be impacting the SBET. However, it appears that variations in the source of fly ash and synthesis conditions, such as temperatures (60, 80, and 100 °C), NaOH content and molarity, and activation time, have a greater impact on SBET, as evidenced by the wide range of surface areas observed (from 3.62 m^2/g to 61.638 m^2/g) [30,31]. This variation highlights the significant impact of both synthesis conditions and fly ash characteristics on the final properties of the zeolites. While a larger surface area generally provides more sites for adsorption, the relationship between SBET and cesium adsorption is not straightforward, as other factors, such as surface charge and ion-specific interactions, also play crucial roles.

Comparing the CEC values with the cesium content in the contaminated zeolite samples (Cs-STD-4A, Cs-ZCFA, and Cs-ZSCBA) can provide insights into their respective adsorption capacities. While there is not a direct correlation between CEC and cesium adsorption due to the complex nature of adsorption processes, we can infer some relationships.

Zeolites with higher CEC values, such as STD-4A (3.14 meq g^{-1}) and ZCFA (3.15 meq g^{-1}), might exhibit enhanced cesium adsorption capabilities due to a greater number of exchangeable sites available for ion uptake. This suggests that these zeolites could effectively adsorb and retain cesium ions from the solution, leading to higher levels of adsorbed cesium compared to zeolites with lower CEC values.

However, the relationship between CEC and cesium adsorption is not solely determined by CEC values. Other factors, including Si/Al ratio, surface area, pore size distribution, and specific interactions between cesium ions and zeolite surfaces, also play significant roles in dictating cesium adsorption capacities.

Therefore, while higher CEC values may generally indicate greater potential for cesium adsorption, the actual adsorption performance can vary based on these complex interplays of factors. For instance, despite its lower CEC value, ZSCBA (2.31 meq g^{-1}) exhibited the highest cesium content among the contaminated zeolite samples. This finding indicates that the difference in Si/Al ratio associated with the presence of iron and calcium in lower quantities (compared to ZCFA), may have contributed to the superior selectivity of ZSCBA towards cesium ion adsorption.

Figures 8 and 9 present the EDS spectra and mapping images of the zeolites before and after the adsorption. The EDS analysis was focused on a single cube from each zeolite sample, and the intensities were normalized to compare the spectra. The presence of Si, Al, Na, and O in the zeolites was consistent before and after the ion exchange process. The spectra clearly show the variation in Si/Al ratios, as previously reported in Table 1. ZCFA exhibited the most significant disproportion between Al (1.5 keV) and Si (1.75 keV), while a more balanced Si/Al ratio, closer to 1, was observed for ZSCBA. Notably, a marked reduction in sodium content, alongside the emergence of cesium signals, is evident for all zeolites after the adsorption experiments, indicating successful cesium uptake.

The mapping images in Figure 9 reveal that Si, Al, Na, and O are uniformly distributed within the zeolite lattices. The presence of Cs, distributed similarly to Na in the adsorbed zeolites, indicates a homogenous adsorption process.
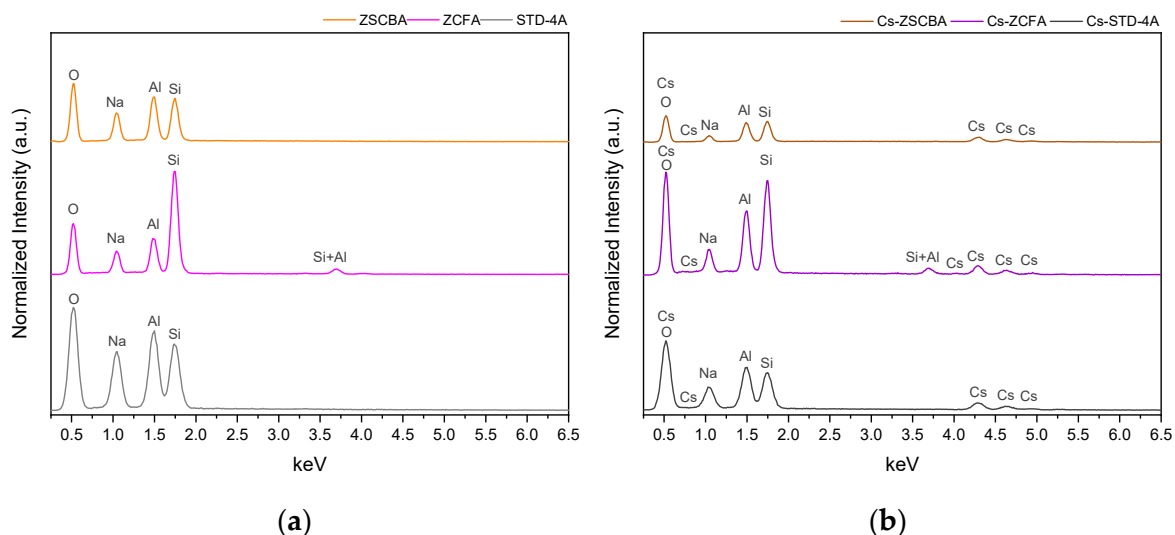
Figure 8. EDS point analysis spectra of the zeolites (**a**) before and (**b**) after adsorption.

Figure 10 presents the X-ray diffraction patterns of the zeolites after the adsorption experiments.

The observed intensity variations in the diffractogram of samples containing Cs^+, particularly attributed to the high X-ray absorption coefficient of Cs^+ ions, aligned with previous findings in the literature. This behavior underscores the high selectivity of Cs^+ ions for zeolite type A, wherein Cs^+ ions replace Na^+ ions (ionic radius = 0.095 nm) in the zeolite structure, maintaining charge balance [32,33]. Despite these changes in peak intensities and minor lattice distortions resulting from the replacement of Na^+ with Cs^+, the crystalline phase identified after Cs^+ adsorption remains consistent with zeolite 4A.
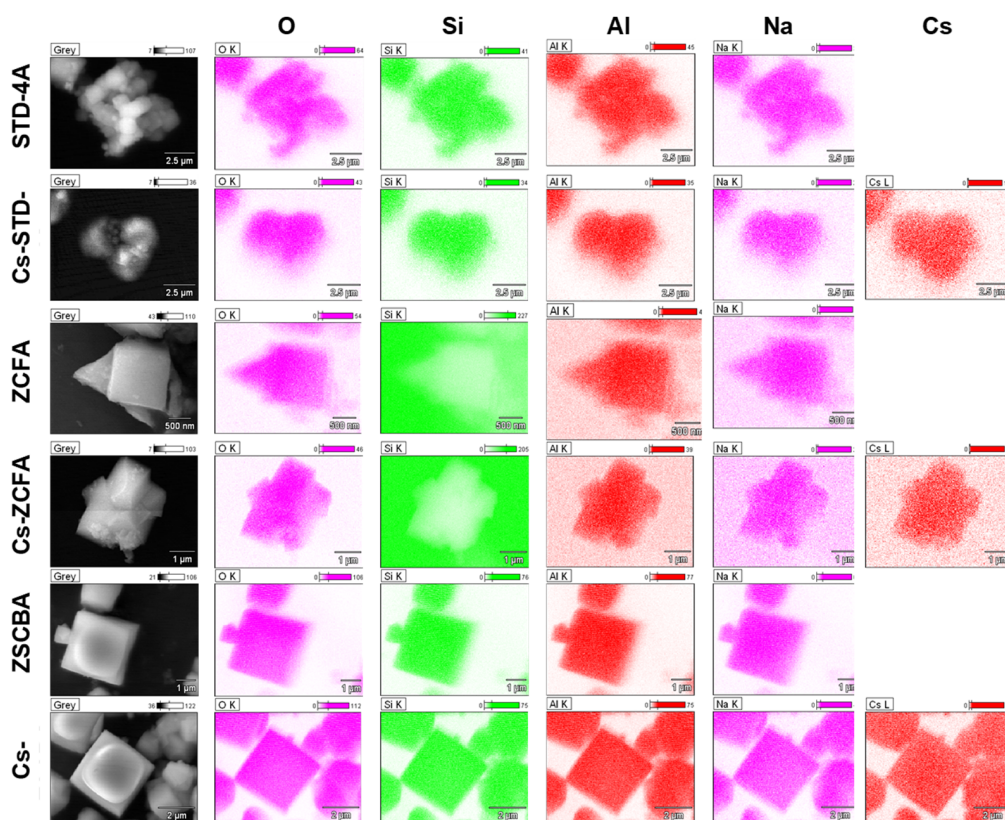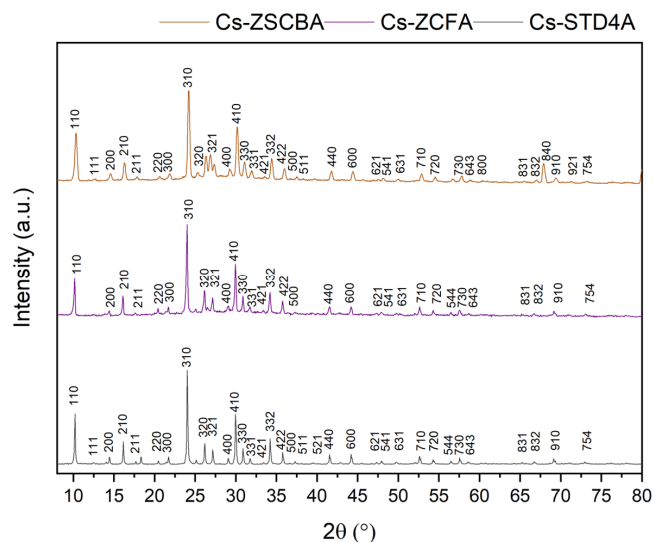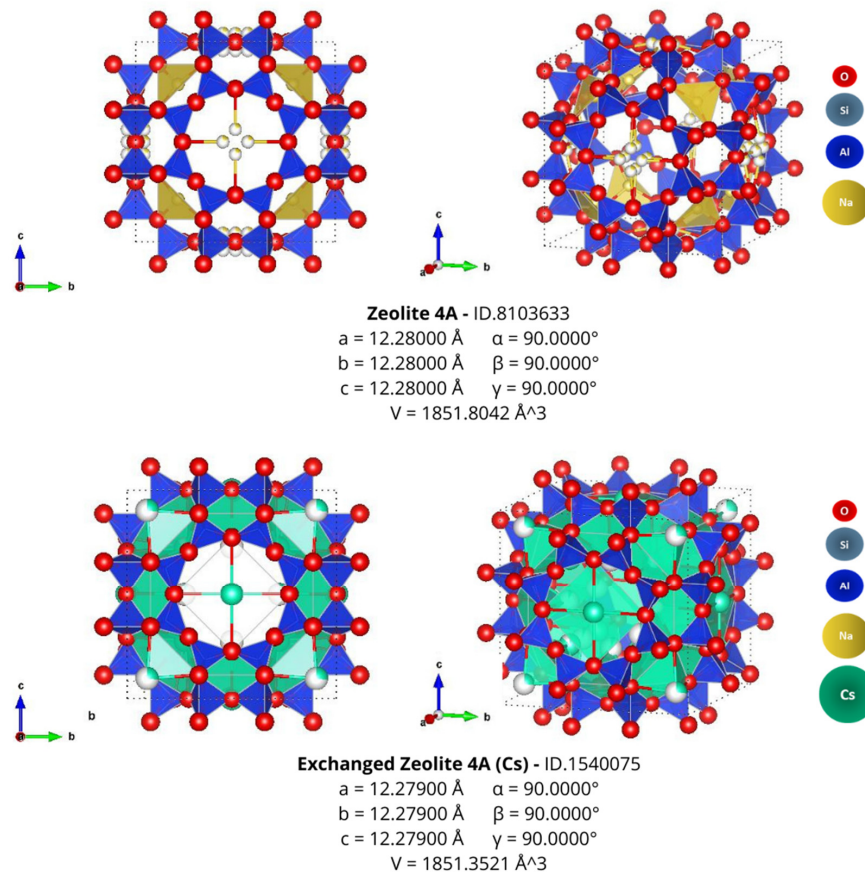

Figure 9. EDS mapping images of the zeolites presenting the elements O, Si, Al, Na, and Cs.

Figure 10. X-ray diffraction patterns of the zeolites after the adsorption experiment (Cs-STD4A, Cs-ZCFA, and Cs-ZSCBA).

Figure 11 provides a schematic representation of the zeolite crystalline structures before and after the adsorption tests, visually illustrating the structural changes occurring during cesium adsorption. The ionic radius of Cs^+ (0.169 nm) allows it to pass through the 8R windows (approximately 0.4 nm in diameter) and occupy the sites within the zeolite framework. The size of the spacing at the center of the 8R window favorably fits the Cs^+ radius [25]. These representations, supported by the XRD data, highlight the structural integrity of the zeolite framework throughout the adsorption process.

Zeolite 4A - ID.8103633

a = 12.28000 Å   α = 90.0000°
b = 12.28000 Å   β = 90.0000°
c = 12.28000 Å   γ = 90.0000°
V = 1851.8042 Å^3

Exchanged Zeolite 4A (Cs) - ID.1540075

a = 12.27900 Å   α = 90.0000°
b = 12.27900 Å   β = 90.0000°
c = 12.27900 Å   γ = 90.0000°
V = 1851.3521 Å^3

Figure 11. Schematic representation of the crystalline structure of the zeolites.

This study demonstrates a viable method for the sustainable utilization of agro-industrial waste as raw materials for zeolite production. This approach minimizes the need for waste disposal and offers versatility for various applications, including water treatment and catalysis.

4. Conclusions

Zeolites from the two different solid wastes, sugarcane bagasse ash (SCBA) and coal fly ash (CFA), were produced using a hydrothermal method. Characterization techniques confirmed the formation of high-purity zeolite, with physicochemical properties comparable to commercial zeolite. The presence of some inherent impurities from ashes impacted the Si/Al ratio and, consequently, influenced the cation exchange capacities (CEC).

Zeolite derived from sugarcane bagasse ash (ZSCBA) achieved a maximum adsorption of 33.4 wt% of cesium, obtained using neutron activation analysis (NAA), and surpassing both the zeolite from coal fly ash (ZCFA) (26.0 wt%) and the commercial zeolite (27.9 wt%). The superior performance of ZSCBA can be attributed to its distinct Si/Al ratio and lower levels of impurities, highlighting that the adsorption process is governed by a complex interplay of factors beyond CEC.

Still, both SCBA and CFA present distinct advantages as raw materials for zeolite synthesis. The choice of the most suitable precursor depends on various factors, including wastewater composition and local availability and cost. Further research should focus on optimizing synthesis parameters to tailor the properties of zeolite derived from both SCBA and CFA, maximizing their efficiency and safety for specific wastewater treatment applications.

Author Contributions: Conceptualization, M.S.A. and D.A.F.; Methodology, J.C.I.; Validation, D.C.-S.; Formal analysis, M.S.A.; Writing—original draft, M.S.A.; Writing—review & editing, D.C.-S., D.A.F. and S.M.C.; Supervision, D.A.F. and S.M.C.; Project administration, D.A.F. and S.M.C.; Funding acquisition, D.A.F. and S.M.C. All authors have read and agreed to the published version of the manuscript.

Data Availability Statement: Data are contained within the article.

Conflicts of Interest: The authors declare no conflict of interest.

References

1. Barbosa, F.O.; de Souza, D.M.T.; Campos, G.O.; de Almeida Carvalho, A.L.F.; de Oliveira, B.M.; Caminha, G.C.; de Araújo, L.V.; de Almeida, C.F. Portfólio de patentes em tecnologias nucleares e outras tecnologias competitivas da CNEN com foco na sustentabilidade/CNEN's patent portfolio on nuclear and other competitive technologies with a focus on sustainability. *Braz. J. Dev.* **2021**, *7*, 187–210. [CrossRef]
2. ReliefWeb. Climate Change and Nuclear Power 2022: Securing Clean Energy for Climate Resilience—World. Available online: https://reliefweb.int/report/world/climate-change-and-nuclear-power-2022-securing-clean-energy-climate-resilience (accessed on 26 October 2023).
3. Kumari, S.; Chowdhry, J.; Kumar, M.; Chandra Garg, M. Zeolites in wastewater treatment: A comprehensive review on scientometric analysis, adsorption mechanisms, and future prospects. *Environ. Res.* **2024**, *260*, 119782. [CrossRef] [PubMed]
4. Li, J.; Gao, M.; Yan, W.; Yu, J. Regulation of the Si/Al ratios and Al distributions of zeolites and their impact on properties. *Chem. Sci.* **2023**, *14*, 1935–1959. [CrossRef] [PubMed]
5. Derbe, T.; Temesgen, S.; Bitew, M. A Short Review on Synthesis, Characterization, and Applications of Zeolites. *Adv. Mater. Sci. Eng.* **2021**, *2021*, 6637898. [CrossRef]
6. Zhang, W.; Zhang, T.; Lv, Y.; Jing, T.; Gao, X.; Gu, Z.; Li, S.; Ao, H.; Fang, D. Recent Progress on the Synthesis and Applications of Zeolites from Industrial Solid Wastes. *Catalysts* **2024**, *14*, 734. [CrossRef]

7. Murukutti, M.K.; Jena, H. Synthesis of nano-crystalline zeolite-A and zeolite-X from Indian coal fly ash, its char-acterization and performance evaluation for the removal of Cs+ and Sr2+ from simulated nuclear waste. *J. Hazard. Mater.* **2022**, *423*, 127085. [CrossRef]

8. Nasser, G.A.; Muraza, O.; Nishitoba, T.; Malaibari, Z.; Yamani, Z.H.; Al-Shammari, T.K.; Yokoi, T. Microwave-Assisted Hydrothermal Synthesis of CHA Zeolite for Methanol-to-Olefins Reaction. *Ind. Eng. Chem. Res.* **2019**, *58*, 60–68. [CrossRef]

9. Park, J.W.; Kim, S.S.; Lee, W.K.; Lee, C.H. Optimization of crystallization parameters for synthesis of zeolitic materials from coal fly ash using fusion/hydrothermal method. *Mol. Cryst. Liq.* **2020**, *704*, 136–144. [CrossRef]

10. Panitchakarn, P.; Laosiripojana, N.; Viriya-umpikul, N.; Pavasant, P. Synthesis of high-purity Na-A and Na-X zeolite from coal fly ash. *J. Air Waste Manag. Assoc.* **2014**, *64*, 586–596. [CrossRef]

11. Kotova, O.B.; Shabalin, I.L.; Shushkov, D.A.; Kocheva, L.S. Hydrothermal synthesis of zeolites from coal fly ash. *Adv. Appl. Ceram.* **2016**, *115*, 152–157. [CrossRef]

12. Fan, Y.; Huang, R.; Liu, Q.; Cao, Q.; Guo, R. Synthesis of zeolite A from fly ash and its application in the slow release of urea. *Waste Manag.* **2023**, *158*, 47–55. [CrossRef] [PubMed]

13. Zhang, J.; Li, Z.; Yi, H.; Tang, X.; Cheng, H.; Yu, Q. Synthesis and application prospect of small-pore zeolites in vehicle exhaust purification. *Fuel* **2023**, *348*, 128577. [CrossRef]

14. Ybañez, Q.; Sanchez, P.; Buladaco, M.S., II; Rosales, J.E. Synthesis and Characterization of Nanozeolite from Sugarcane Bagasse Ash and Its Nutrient Loading Potential. *Philipp. Agric. Sci.* **2022**, *105*, 317–324. [CrossRef]

15. Belviso, C. State-of-the-art applications of fly ash from coal and biomass: A focus on zeolite synthesis processes and issues. *Prog. Energy Combust. Sci.* **2018**, *65*, 109–135. [CrossRef]

16. Zou, Q.; Lin, W.; Xu, D.; Wu, S.; Mondal, A.K.; Huang, F. Study the effect of zeolite pore size and acidity on the catalytic pyrolysis of Kraft lignin. *Fuel Process Technol.* **2022**, *237*, 107467. [CrossRef]

17. de Carvalho Izidoro, J.; Fungaro, D.A.; Cataldo, E. Zeolites synthesized from agro-industrial residues applied in agriculture: A review and future prospects. *Soil. Use Manag.* **2024**, *40*, e13003. [CrossRef]

18. Izidoro, J.d.C.; Fungaro, D.A.; Abbott, J.E.; Wang, S. Synthesis of zeolites X and A from fly ashes for cadmium and zinc removal from aqueous solutions in single and binary ion systems. *Fuel* **2013**, *103*, 827–834. [CrossRef]

19. Izidoro, J.d.C.; Fungaro, D.A.; dos Santos, F.S.; Wang, S. Characteristics of Brazilian coal fly ashes and their syn-thesized zeolites. *Fuel Process Technol.* **2012**, *97*, 38–44. [CrossRef]

20. de Carvalho Izidoro, J.; Kim, M.C.; Bellelli, V.F.; Pane, M.C.; Botelho Junior, A.B.; Espinosa, D.C.R.; Soares Tenório, J.A. Synthesis of zeolite A using the waste of iron mine tailings dam and its application for industrial effluent treatment. *J. Sustain. Min.* **2019**, *18*, 277–286. [CrossRef]

21. Izidoro, J.; Castanho, D.; Rossati, C.; Fungaro, D.; Guilhen, S.; Nogueira, T.; De Fátima Andrade, M. Application of high-purity zeolite a synthesized from different coal combustion by-products in carbon dioxide capture. *Int. J. Envirion. Manag. Mit. Rec.* **2019**, *2*, 215–228. [CrossRef]

22. Patel, H. Environmental valorisation of bagasse fly ash: A review. *RSC Adv.* **2020**, *10*, 31611–31621. [CrossRef]

23. Praipipat, P.; Ngamsurach, P.; Roopkhan, N. Zeolite A powder and beads from sugarcane bagasse fly ash modified with iron(III) oxide-hydroxide for lead adsorption. *Sci. Rep.* **2023**, *13*, 1873. [CrossRef]

24. Praipipat, P.; Ngamsurach, P.; Sanghuayprai, A. Modification of sugarcane bagasse with iron(III) oxide-hydroxide to improve its adsorption property for removing lead(II) ions. *Sci. Rep.* **2023**, *13*, 1467. [CrossRef]

25. Tian, Q.; Sasaki, K. Application of fly ash-based materials for stabilization/solidification of cesium and strontium. *Environ. Sci. Pol. Res.* **2019**, *26*, 23542–23554. [CrossRef]

26. Mozgawa, W.; Król, M.; Dyczek, J.; Deja, J. Investigation of the coal fly ashes using IR spectroscopy. *Spectrochim. Acta A Mol. Biomol. Spectrosc.* **2014**, *132*, 889–894. [CrossRef]

27. Smith, J.V.; Dowell, L.G. Revised crystal structure of dehydrated Na-Type A zeolite. *Z. Kristallogr. Cryst. Mater.* **1968**, *126*, 135–142. [CrossRef]

28. Król, M.K.; Jeleń, P. The Effect of Heat Treatment on the Structure of Zeolite A. *Materials* **2021**, *14*, 4642. [CrossRef]

29. Titus, M. Preparation, Characterization and Modeling of Zeolite NaA Membranes for the Pervaporation Dehydration of Alcohol Mixtures. Ph.D. Thesis, Universitat de Barcelona, Barcelona, Spain, 2006.

30. Vegere, K.; Kravcevica, R.; Krauklis, A.E.; Juhna, T. Comparative study of hydrothermal synthesis routes of zeolite A. *Mater. Today Proc.* **2020**, *33*, 1984–1987. [CrossRef]

31. Koshlak, H. Synthesis of Zeolites from Coal Fly Ash Using Alkaline Fusion and Its Applications in Removing Heavy Metals. *Materials* **2023**, *16*, 4837. [CrossRef]

32. Al Ezzi, A.; Ma, H. Equilibrium adsorption isotherm mechanism of water vapor on zeolites 3A, 4A, X, and Y. In Proceedings of the ASME International Mechanical Engineering Congress and Exposition, Proceedings (IMECE), Tampa, FL, USA, 3–9 November 2017; p. 6. [CrossRef]

33. Pérez-Botella, E.; Valencia, S.; Rey, F. Zeolites in Adsorption Processes: State of the Art and Future Prospects. *Chem. Rev.* **2022**, *122*, 17647–17695. [CrossRef]